

Annealing-based Manipulation of Thermal Phonon Transport from Light Emitting Diodes to Graphene

Sang-Hyuk Park,¹ Hun Lee,¹ Sehyuk Lee,¹ Austin J. Minnich,² Woo-Lim Jeong,¹ Dong-Seon Lee,¹ Soon-Sung So,³ Joo-Hyoung Lee,³ Young Min Song,¹ and Young-Dahl Jho^{1, a)}

¹⁾*School of Electrical Engineering and Computer Science, Gwangju Institute of Science and Technology, Gwangju 61005, Korea*

²⁾*Division of Engineering and Applied Science, California Institute of Technology, Pasadena, California 91125, United States*

³⁾*School of Materials Science and Engineering, Gwangju Institute of Science and Technology, Gwangju 61005, Korea*

(Dated: 29 November 2021)

We demonstrate that the thermal boundary conductivity (TBC) between graphene and GaN-based light-emitting diodes (LEDs) can be manipulated through thermal annealing, which is verified by measuring the acoustic phonons after reflection at the interface. Thermal annealing affects the interfacial morphology as evaluated by both the Raman spectra and the spatial profile of the graphene wrinkles in atomic force microscopy. By tracing the phase of ultrafast acoustic oscillations on the basis of the pump-probe scheme, we extract the phonon reflection coefficient at the interface as a function of annealing temperatures up to 400 °C. Specifically, the phase shift of transient phononic oscillations at the graphene/LED interface conveys the photoelastic response during the phonon transfer process and can be used for extracting the interfacial coupling rate which is strongly enhanced around ~ 200 °C. By incorporating the heat capacity and the interfacial coupling constants into TBC, along with analytical modeling based on the phonon reflection coefficients, we show that the TBC increases with the minimized surface roughness of graphene side at 200 °C. This new comprehensive TBC extraction scheme could spark further discussion on improving the heat dissipation of LEDs.

I. INTRODUCTION

In accordance with the need for efficient thermal management owing to the aggressive downsizing of the devices, graphene has attracted a great deal of attention as a heat-spreading layer¹⁻⁴ due to the remarkable in-plane thermal conductivity (κ) up to 5300 W/mK⁵. However, when graphene is supported on a substrate, the ultra-high κ drops to approximately 600 W/mK possibly because of phononic leakage and scattering across the interface⁶. In addition, the thermal properties of graphene are sensitive to defects such as vacancies⁷, isotropic impurities⁸, and stacking faults⁹, which reduce the κ of graphene.

In addition, owing to its inherent stretchability without fracture and weak van der Waals (vdW) coupling, out-of-plane deformations associated with local bending, such as wrinkling¹⁰, also severely affect the heat transfer properties. The wrinkling of graphene can be controlled by the thermal annealing treatment¹¹ because it is related to the mismatch of the thermal expansion coefficient between graphene and the substrate¹². Recently, thermal conduction has been studied theoretically in terms of graphene wrinkling^{13,14}. Important observations here include that κ decreases owing to an increase in the phonon scattering rate with the degree of wrinkling. Although some studies have examined the in-plane thermal transport across the wrinkles in graphene¹⁵, investigations on the cross-plane thermal transport at the interface between graphene and the substrate are still lacking.

In this study, we demonstrate a novel approach for extracting thermal boundary conductance (TBC) at the interface

between graphene and light-emitting diodes (LEDs) by analyzing the phase shift of acoustic (AC) phonon oscillations. Phase analysis is incorporated into ultrafast acoustics to quantify the phonon reflection coefficients from which both vdW coupling constants and TBC values are successively extracted. As a result, the TBC value from the 200 °C annealed sample was evaluated to be ~ 13 times greater than that of the unannealed sample.

II. EXPERIMENTAL METHODS

The graphene was grown by chemical vapor deposition (CVD) on Cu foil and transferred onto GaN-based LED structures based on the conventional method assisted by poly-methyl methacrylate (PMMA), as illustrated in Fig. 1. The detailed procedures can be sequenced as follows: (a) single-layer graphene was grown on Cu foil using CVD; (b) the graphene on Cu foil was coated with PMMA as a supporting layer; (c) the graphene on the other side of the Cu foil was removed by reactive ion etching, and the Cu foil was then eliminated by $(\text{NH}_4)_2\text{S}_2\text{O}_8$; (d) subsequently, the PMMA/graphene was transferred onto the LED; (e) the PMMA was dissolved in acetone and then removed; (f) the graphene/LED structures were annealed by a rapid thermal annealing system under N_2 ambient for 60 min at different annealing temperatures of 200 and 400 °C.

Thermal annealing can eliminate polymeric residues^{16,17} and concurrently improve the interfacial coupling between graphene and the substrate¹⁸. To quantitatively evaluate the annealing-induced surface morphology on the graphene side, Raman spectroscopy was first performed using an excitation laser centered at ~ 514 nm with a spot size on the order of ~ 1

^{a)}Electronic mail: jho@gist.ac.kr

This is the author's peer reviewed, accepted manuscript. However, the online version of record will be different from this version once it has been copyedited and typeset.
PLEASE CITE THIS ARTICLE AS DOI: 10.1063/1.50069466

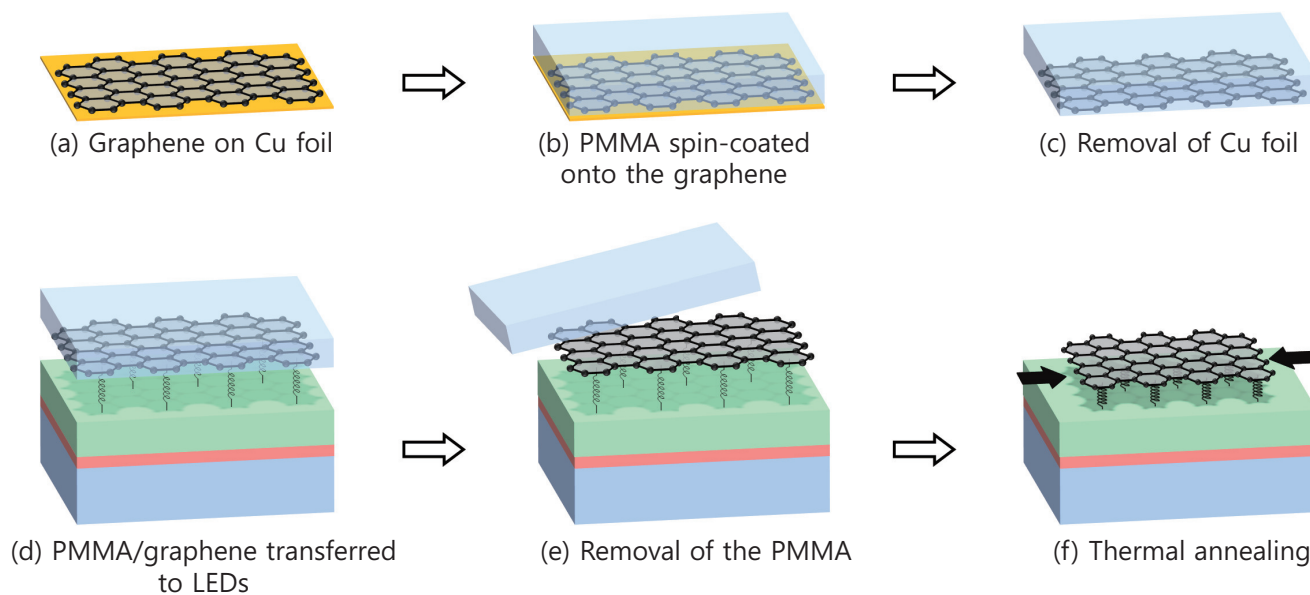


FIG. 1. Schematic for the transfer process of chemical vapor deposition (CVD)-grown monolayer graphene. (a) Single-layer graphene on Cu foil was prepared. (b) Polymethyl methacrylate (PMMA) was spin-coated onto graphene on Cu foil. (c-d) PMMA-assisted graphene was transferred from the Cu foil to the GaN-based LEDs. (e) PMMA was removed. Then, (f) graphene on LEDs is annealed by a rapid thermal annealing system at different temperatures of 200 and 400 °C.

μm . To avoid laser-induced heating and deformation, the excitation power was kept below 0.1 mW. The Raman spectrum was mapped over a region of $100 \mu\text{m} \times 100 \mu\text{m}$ to examine the local strain distribution. The height of graphene was traced using atomic force microscopy (AFM) to evaluate the surface roughness and spatial distribution of wrinkles as a function of the annealing temperature.

To measure the phonon transport at the interface between graphene and the GaN surface, we traced the phase of longitudinal AC (LA) wavepackets measured via ultrafast acoustics upon UV laser excitation with a pulse width of ~ 150 fs and a spot size of $20 \mu\text{m}$, similar to our previous work.¹⁹ The periodically strain-modulated AC transducer layer, comprising eight pairs of 2-nm-thick $\text{In}_{0.15}\text{Ga}_{0.85}\text{N}$ quantum wells and 6-nm-thick GaN barriers, was encased by 100-nm-thick *p*-doped GaN layer on top and a $\sim 4\text{-}\mu\text{m}$ -thick *n*-doped layer underneath, all grown along the *c*-axis. Differential reflectivity spectra transiently recorded the Brillouin oscillations in line with LA propagation dynamics from the epicenter to the graphene side at room temperature under the normal incidence of pump and probe pulses with collinear polarization. Considering the pump fluence of $\sim 80 \mu\text{J}/\text{cm}^2$ at a wavelength of 400 nm, we selectively screened the tensile strains only in quantum wells. Thus, a LA wavepacket was initiated, preserving the spatial distribution of multiple quantum wells spanning 56 nm, the initial phase of which were in good agreement with the displacively generated tensile strain pulses²⁰. The phase values after diffusive reflection at the interface can then be extracted as a function of the annealing temperature. To cover the two-dimensional distribution of the interfacial adhesion strength according to the local variation of graphene morphol-

ogy, the phase was extracted from 25 different positions over an area of $100 \mu\text{m} \times 100 \mu\text{m}$.

III. RESULTS AND DISCUSSION

A. Surface morphology of graphene

Delamination from the substrate surface is often observed owing to the spatially non-uniform bonding characteristics between graphene and substrates.^{21–23} Thermal annealing can affect the delamination nature at the interface by changing the vdW coupling constant, k_{vdW} , accompanied by compressive strain applied to the graphene side due to the severe mismatch in the thermal expansion coefficient between graphene ($\sim -8 \times 10^{-6} \text{K}^{-1}$)²⁴ and the LED side ($\sim 5 \times 10^{-6} \text{K}^{-1}$)²⁵. Considering the well-established linear strain dependence of the 2D peak shift in comparison to strain-free exfoliated graphene^{22,26,27}, we can use the spatial variation of 2D peak positions to contour the strain profiles. In this respect, the Raman spectra were scanned over the area of $100 \mu\text{m} \times 100 \mu\text{m}$ near the 2D peak, as shown in Fig. 2(a-c). The contour plots of the 2D peak, in this way, overview the spatial distribution of the corresponding compressive strain for each sample. In graphene after annealing treatment, a region with blue-shifted 2D peaks than before annealing was prominently revealed, which was indicated by the dark reddish contrast in line with increasing compressive strain.

Figure 2(d) shows the representative Raman spectra of graphene on GaN-based LEDs after thermal annealing. In general, the Raman spectra of graphene on LEDs contained

This is the author's peer reviewed, accepted manuscript. However, the online version of record will be different from this version once it has been copyedited and typeset.
PLEASE CITE THIS ARTICLE AS DOI: 10.1063/1.50069466

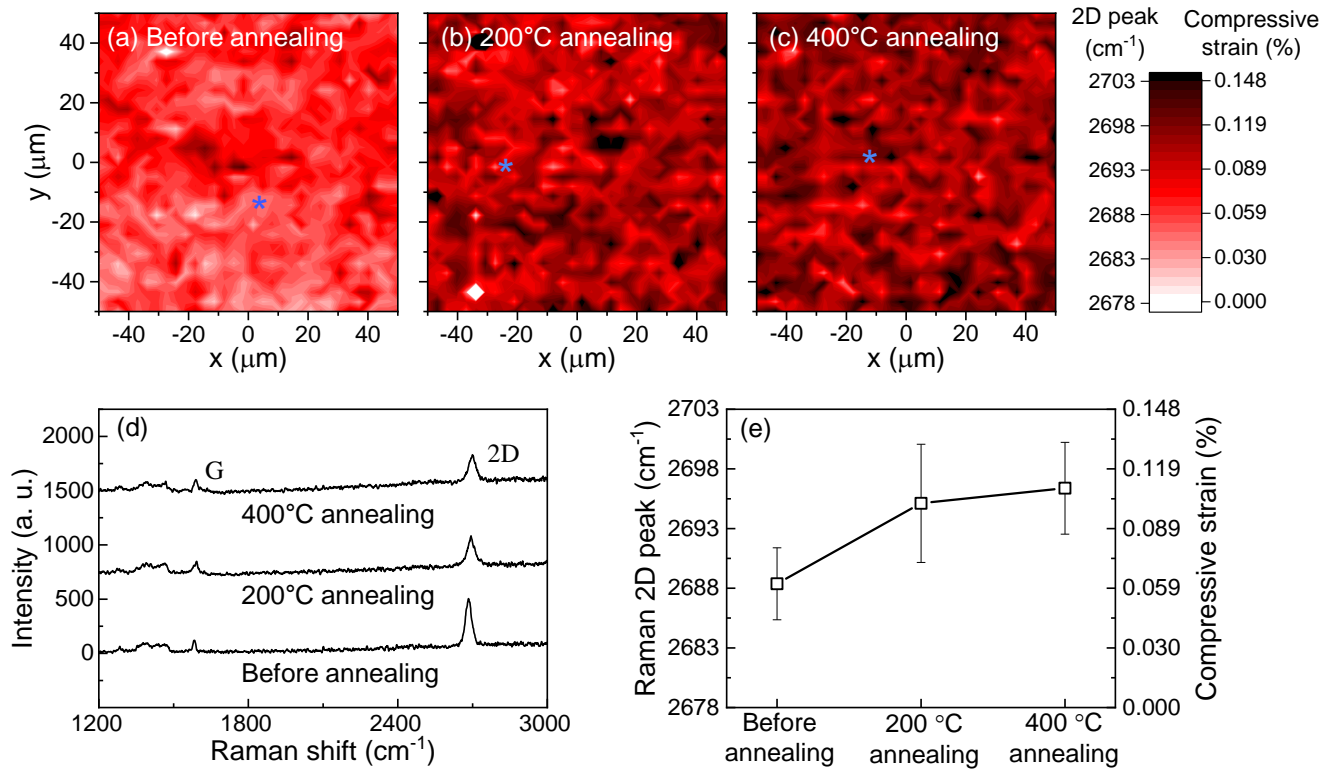


FIG. 2. (a-c) Raman maps for 2D-band obtained from graphene on GaN-based LEDs with different annealing temperature; (a) before annealing, (b) 200 °C annealing, and (c) 400 °C annealing. (d) Raman spectra with various annealing temperatures, representatively measured at locations marked with asterisks in Fig. 1(a-c). (e) The mean values (scatter) and standard deviations (error bars) of the Raman 2D peaks, converted into compressive strain applied to the graphene (y-axis on the right) for various annealing temperatures.

two prominent peaks, denoted as G-($\sim 1350 \text{ cm}^{-1}$) and 2D-band ($\sim 2680 \text{ cm}^{-1}$). The lineshapes display the typical features of single-layer graphene with high crystallinity²⁸. Notably, in Fig. 2 (d), the 2D peak is blue-shifted with the thermal annealing temperature. The corresponding mean values and standard deviation of the 2D peak positions are indicated by scatters and error bars in Fig. 2(e), where the 2D peak positions were converted into strain magnitude as indicated on the right side of the y-axis. Before annealing, graphene had a compressive strain of $\sim 0.06\%$, which occurred between the graphene and Cu foil during synthesis.¹² The compressive strain of graphene increased to $\sim 0.10\%$ after 200 °C annealing treatment. The compressive strain did not increase linearly with the annealing temperature, and the compressive strain of graphene in the sample after annealing at 400 °C was saturated around $\sim 0.11\%$. Looking at the graphene 2D peak without annealing in Fig. 2(a) from the perspective of the spatial distribution of strain, the compressive strain distribution on the order of $\sim 0.06\%$ was relatively uniform over the entire area, whereas the dark red region with enhanced compressive strain in Fig. 2(b,c) after annealing was found to be somewhat random. In the case of annealing at 400 °C, the distribution of the compressively strained region colored in dark red only slightly increased compared to the case of 200 °C. This saturation trend of compressive strain, which appears despite the

sharp increase in the annealing temperature, may be a result of strain relaxation due to the wrinkling of graphene.^{29,30}

In order to inspect the morphological changes of graphene in relation to the compressive strain formation after the annealing process, AFM was employed with a scanning area of $5 \mu\text{m} \times 5 \mu\text{m}$ in Fig. 3. The line profiles of the bare LED sample in Fig. 3(a) and graphene on LEDs in Fig. 3(b-d) along the solid arrows are shown in Fig. 3(e-h). As shown in Fig. 3(a), the bare GaN has a roughness (δ_{GaN}) of $\sim 0.22 \text{ nm}$, indicating that the surface of GaN is atomically flat from the pseudomorphic growth. In the case of graphene before annealing, a height fluctuation of $\sim 2 \text{ nm}$ with sinusoidal pattern was observed, as shown in Fig. 3 (f), which could be ascribed to the residual stress applied during CVD-growth on the Cu foil¹² or transfer process using PMMA¹⁶. Compared to the bare LED shown in shades of green in Fig. 3(f), the area with the lowest height adheres well to the substrate, while the area with the higher height indicates delamination from the substrate. In this case, it can be assumed that the smallest distance h_0 between the graphene and the LED is the same as the value in the case where the graphene is sandwiched by crystalline materials to prevent height fluctuation³¹. After the annealing treatment, sharp wrinkles appeared at quasi-periodic intervals along a certain direction. As the annealing temperature increased from 200 to 400 °C, the spatial spacing

This is the author's peer reviewed, accepted manuscript. However, the online version of record will be different from this version once it has been copyedited and typeset.
PLEASE CITE THIS ARTICLE AS DOI: 10.1063/1.50069466

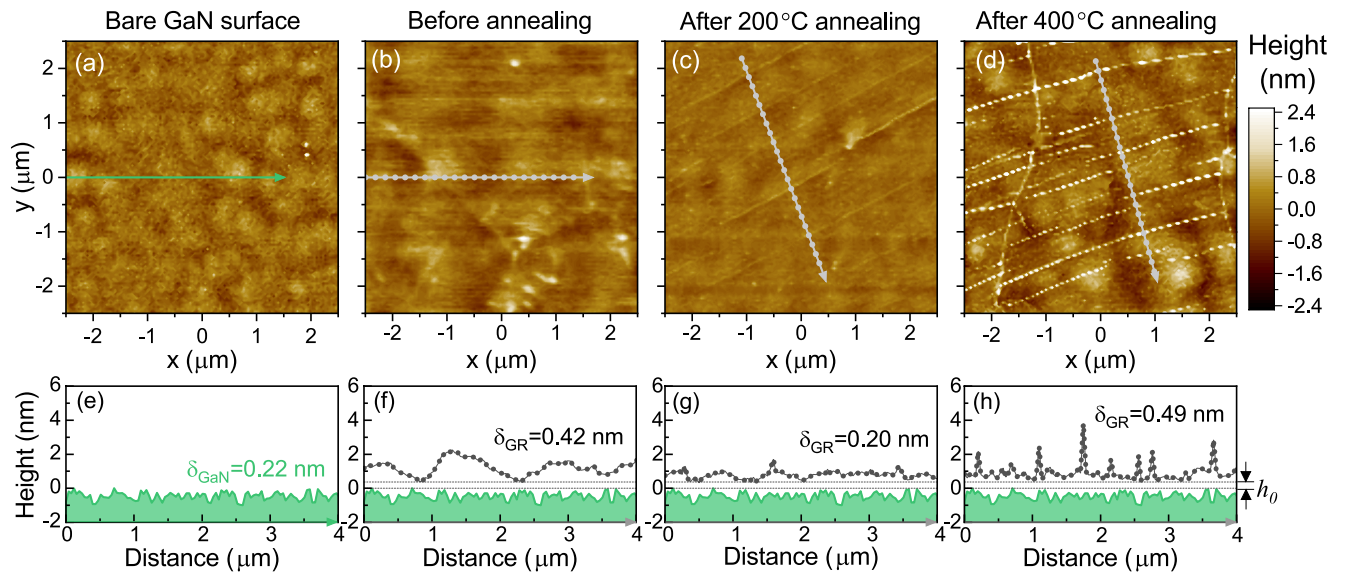


FIG. 3. Atomic force microscopy images of (a) GaN substrate and (b-d) graphene on GaN substrate with different annealing temperature; (b) before annealing and after annealing at (c) 200 °C and (d) 400 °C. (e-h) The line profiles along the line indicated in (a-d). h_0 represents the minimum interfacial separation between the graphene and the GaN surface.

of wrinkles shortened from ~ 780 to ~ 550 nm, and the height of the wrinkles increased simultaneously. For 200 °C annealing, the wrinkle height was less than 1 nm with the surface roughness being minimized. In the sample annealed at 400 °C, the wrinkle height increased significantly to ~ 4 nm. The specific surface roughness (δ_{GR}) of graphene was measured to be approximately 0.42 nm without annealing, and decreased to 0.20 nm at 200 °C at first, then increased to 0.49 nm at 400 °C. Remarkably, the average value of compressive strain for each sample itself did not directly correlate with surface roughness. This is because the spatial distribution of strain is not uniform, and thermal expansion and lattice constant mismatch have a complicated effect on the coupling strength.

B. Characterization of interfacial thermal transport

Ultrafast acoustics, as the most common framework for measuring AC phonon dynamics before thermalization, has been well established based on the relation between the change in the refractive index of the medium (Δn) and the phonon-induced localized strain (η) in the harmonic regime ($\eta \ll 1$). Then, the coherent AC oscillations in the differential reflectivity spectra ($\Delta R/R$) are approximated as $\propto \cos(2\pi f_B t + \phi_0)$ ^{32,33}, where f_B is the Brillouin frequency. The residual phase ϕ_0 is preset to $2nkz_0$ by the epicenter of the AC phonons (z_0 , the center of a quantum well in our case) and a probe beam wavenumber (k). The amplitude of the transient Brillouin oscillation is proportional to the amplitude of η . Such ultrafast acoustics schemes have recently been employed for characterizing interfacial properties such as vdW interfaces^{34,35} and atomically thin interlayers.^{36–38}

From an analytical perspective, the AC transport at the in-

terface is still almost imperceptible from the amplitude of $\Delta R/R$, which already exhibits various complex effects with thermalization and probe wavelength absorption over time. In contrast, however, the phase of $\Delta R/R$ clearly represents the temporal evolution of the AC component as long as the associated AC wavepackets consist of a bipolar strain composition with η_T from QW and η_C after reflection²⁰. When η_T - and η_C -guided photoelastic modulations are superimposed on $\Delta R/R$, additional composition-dependent phase modulation $\phi_{C/T}$ appears. Thus, $\Delta R(t)/R = \Delta^{\eta_T} R(t)/R + \Delta^{\eta_C} R(t)/R \propto \cos(2\pi f_B t + \phi_0 + \phi_{C/T})$. Here, the bipolarity-induced phase component, $\phi_{C/T}$, is formulated as

$$\phi_{C/T} = \tan^{-1} \left[\frac{\sin(2nk(z_C - z_T))}{\cos(2nk(z_C - z_T)) - (\eta_C/\eta_T)^{-1}} \right], \quad (1)$$

where the amplitudes of η_C and η_T are incorporated into the phase modulation (further mathematical details can be found elsewhere³⁹). Interestingly, the smaller value of η_C/η_T , extracted from $\phi_{C/T}$, implies more efficient phonon transport from the LED to graphene, in addition to the surface scattering rates. Eq. (1), in this way, shows that the phase of the ultrafast acoustics involves the previously belittled characteristics of interfacial phononic transport.

To evaluate the phonon transport from GaN to graphene for each sample with different annealing temperatures, we carefully traced the phase of $\Delta R/R$ near the surfacial reflection point in Fig. 4. At zero time delay, the pump beam excites only the InGaN MQWs in the GaN-based LED structure, which then launches the LA wavepacket with the same amplitudes via piezoelectric screening¹⁹, as illustrated by the reddish rectangular pulse trains in Fig. 4(a). The propagation routes of AC wavepackets, as depicted by black arrows, descend toward the n -GaN side or ascend toward the graphene

This is the author's peer reviewed, accepted manuscript. However, the online version of record will be different from this version once it has been copyedited and typeset.
PLEASE CITE THIS ARTICLE AS DOI: 10.1063/1.50069466

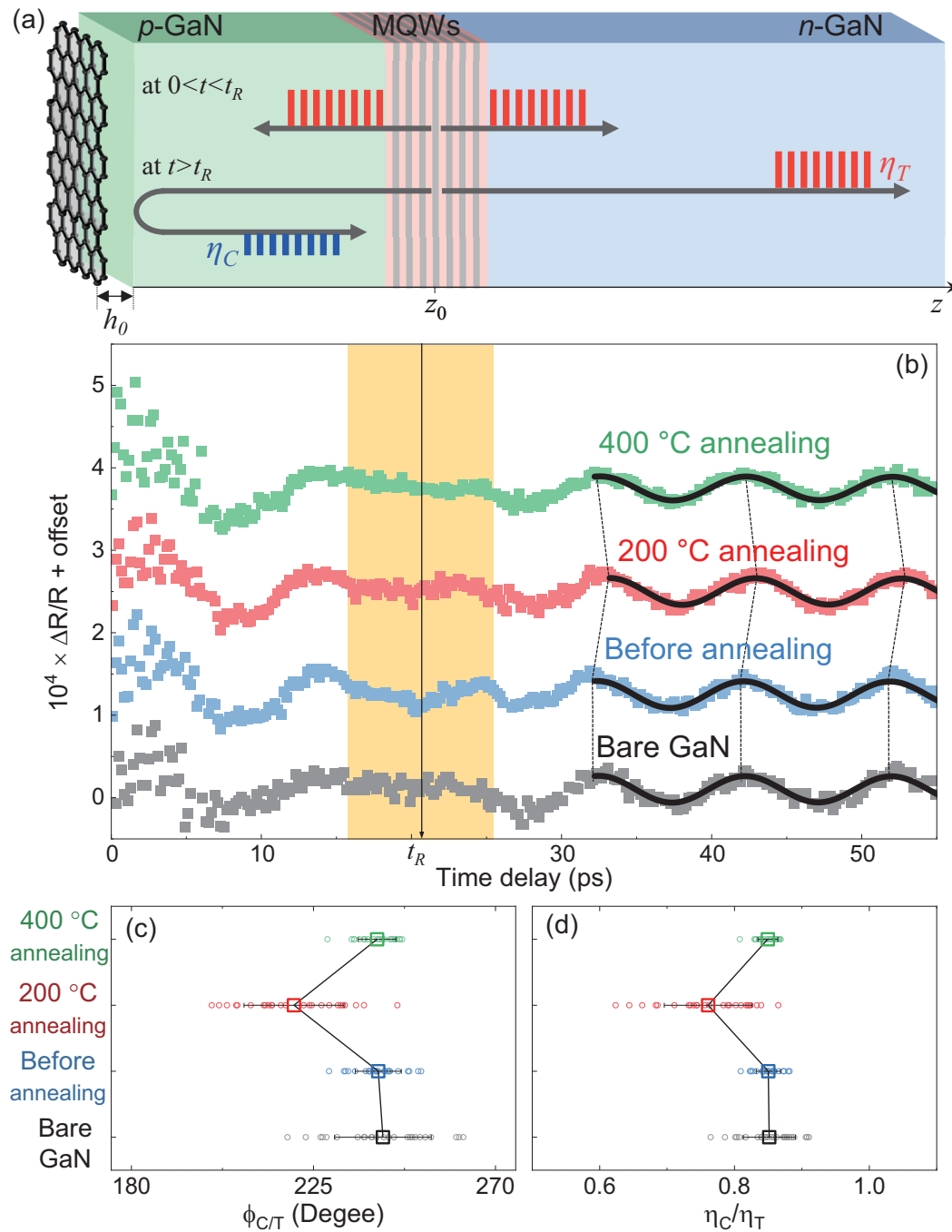


FIG. 4. (a) Schematic diagram of the propagation of acoustic phonon wavepackets in the time range before and after reflection (t_R). (b) Oscillatory parts of the differential reflectivity spectra for different annealing temperatures. The experimental data (scatters) were fitted to cosine waves (solid lines) to extract $\phi_{C/T}$ after surface reflection ($t > t_R$). (c) Trace of $\phi_{C/T}$ values after reflection due to the annealing temperature change. (d) Proportion of oppositely strained components (η_C and η_T), extracted from $\phi_{C/T}$.

side in the time range of $0 < t < t_R$. The ascending AC pulse trains travel through the ~ 100 -nm-thick p-GaN layer, and the reflection at the graphene interface occurs with a period from ~ 17.7 ps to ~ 26.0 ps, considering AC velocity (v_{AC}) of ~ 8 nm/ps in GaN⁴⁰ and the spatial width of AC wavepackets (58 nm). The central reflection time (t_R) was set to be approxi-

mately ~ 21.6 ps, which was further indicated by a straight vertical line within the yellow shade in the transient differential reflectivity spectra of Fig. 2(b). After the reflection, the strain sign of AC wavepackets is reversed to have η_C , possibly with reduced magnitude by the amount of phonon transfer into the graphene side. In this manner, the bipolar compo-

This is the author's peer reviewed, accepted manuscript. However, the online version of record will be different from this version once it has been copyedited and typeset.

PLEASE CITE THIS ARTICLE AS DOI: 10.1063/1.50069466

sitions are established with $z_C - z_T$ fixed for Eq. (1). For bare GaN, a surface with an atomically flat surface acts as a perfect mirror to set η_C/η_T to 1, but a realistic δ_{GaN} value should decrease η_C/η_T via Kapitza diffuse scattering.⁴¹ On the other hand, in the case of the graphene/GaN interface, AC packets from the transducer layer (η_T) can be partially transmitted to the graphene side depending on the interfacial bonding characteristics, and the rest are reflected and overturned to form η_C in our photoelastic detection scheme. For simplicity, by setting the detection range of $\phi_{C/T}$ much shorter than the phononic scattering time (~ 200 ps for 1 THz in the case of doped GaN^{42–45}), the amplitude of initially descending η_T could be adequately presumed to be invariant within the mean free path^{46,47}.

The obtained oscillatory parts of $\Delta R/R$ for bare GaN-based LEDs and graphene on LEDs with different annealing temperatures are shown in Fig. 4(b). The transient Brillouin oscillations, originating from the photoelastic reflections of the probing laser beam off from the AC wavepackets, were clearly demonstrated with well-defined phases. Near $t = t_R$, indicated by the yellow shade, the signal was suppressed because a complex mixture between the partial tensile component before reflection and the compressively deformed portion immediately after reflection constantly changes the strain composition over a rather wide packet width. This indicates that the surface reflection of the AC wavepacket is in progress. The reflection time-domain of the AC wavepacket was estimated to be ~ 7.8 ps, which is in good agreement with the spatial extent of the AC wavepacket.

After reflection ($t > t_R$), as the bipolar packets (consisting of η_C and η_T) propagate in the same direction, $\phi_{C/T}$ can be extracted after subtracting ϕ_0 from the total phase values, as displayed by the scatter plots in Fig. 4(c). To typify locally varying bonding properties, disclosed above based on Figs. 2 and 3, we scanned the $\phi_{C/T}$ values over the graphene surface at 20 different positions. The open squares in Fig. 4(c) represent the average values of $\phi_{C/T}$ from different positions. The average of $\phi_{C/T}$ for LEDs with graphene was then compared to the $\phi_{C/T}$ average for bare LEDs. Both the LEDs before and after annealing at 400 °C showed a slight decrease in $\phi_{C/T}$ compared to the bare LEDs, but the 200 °C annealed sample was significantly decreased in $\phi_{C/T}$. As expected from the measurements of $\phi_{C/T}$, the strain amplitude ratio of η_C/η_T was the lowest with 200 °C annealing, as shown in Fig. 4(d). The strain amplitude ratio of η_C/η_T represents the phononic reflection coefficient r .

The above results suggest that the vdW bonding properties at the graphene/GaN interface affect interfacial phonon transfer. In particular, the importance of controlling nanoscale wrinkles was revealed through the reduced amplitude of the AC wavepacket (η_C) in the 200 °C annealed sample. In its simplest form, the interfacial transmission of AC wavepackets can be formulated based on the AC mismatch model (AMM), which has been applied to a perfectly welded contact⁴⁸ or van der Waals contact⁴⁹. However, because the AC phonon velocity of monolayered graphene cannot be defined along the surface normal direction, the interfacial transport in our structures cannot be intuitively outlined by relying solely on

conventional AMM. To properly formulate acoustic phonon transport at the interface, previous studies have noted that the heat transfer at the interface between graphene and the supporting substrates is dominated by flexural AC (ZA) phonons (i.e., atomic vibrations along the out-of-plane direction).^{6,50,51} In terms of the ZA phonon coupling, we represent η_C/η_T based on frequency-specific evolution as

$$r = \frac{\eta_C}{\eta_T} = \frac{\int_0^\infty \hat{\eta}_T(\omega) \cdot p \cdot e^{-\Delta t/\tau_{ZA}(\omega)} d\omega}{\int_0^\infty \hat{\eta}_T(\omega) d\omega}, \quad (2)$$

where p is the well-known specularity parameter^{52,53}, $e^{-16\pi^2\delta_{\text{GaN}}^2 v_{\text{AC}}^{-2} \omega^2}$, which reveals the dependence on both ω and δ_{GaN} . Within the integration, $\hat{\eta}_T$ denotes the Fourier transform of η_T generated from a 2-nm-thick QW within the transducer layer via displacive piezoelectric screening. Another term of $e^{-\Delta t/\tau_{ZA}}$ in the numerator of Eq. (2) represents the spectral attenuation via the coupling between the LA phonon in the GaN side and the ZA phonon in graphene. In our case, the value of Δt was set to ~ 0.25 ps, corresponding to the temporal width of the AC wavepacket from a single QW. The phonon coupling rate between the LA phonon in GaN and the ZA phonon in graphene is written as^{6,54} $\tau_{ZA}^{-1}(\omega) = \frac{\pi}{2} \frac{D_{\text{GR}}(\omega)}{m_{\text{GR}} m_{\text{GaN}}} \frac{k_{\text{vdW}}^2}{\omega^2}$, where ω is the phonon frequency, $D_{\text{GR}}(\omega)$ is the phonon density of states (DOS) of graphene, and m_{GR} and m_{GaN} are the average weights of atoms on the graphene surface and Ga atoms on the GaN surface, respectively. Here, the ZA phonon coupling rate at the interface, $\tau_{ZA}^{-1}(\omega)$, is linearly proportional to $D_{\text{GR}}(\omega)$, whereas k_{vdW} is the coupling constant, representing the interaction strength between GaN and graphene.

In the process of comparing the experimentally measured phonon reflection coefficient from Fig. 4(d) with the calculation results based on Eq. (2), k_{vdW} involved in τ_{ZA}^{-1} could be extracted by setting it as a variable parameter. Note that we used D_{GR} for perfectly flat graphene for all samples, which allows only k_{vdW} -mediated τ_{ZA}^{-1} as a function of frequency. The phonon DOS of graphene (D_{GR}) is shown in the inset of Fig. 5(a) (see Appendix A for more details regarding the calculation of DOS). According to the variable parameter of k_{vdW} , the AC spectral lineshape can be reproduced, as shown in Fig. 5(a). The yellow solid line in Fig. 5(a) corresponds to $\hat{\eta}_T$, which originated from the Fourier transform of the temporal AC distribution of η_T . The diamond scatters in Fig. 5(a) indicate $\hat{\eta}_C$ for bare GaN after reflection, which exhibits reduced high-frequency components compared to $\hat{\eta}_T$ due to the Kapitza surface scattering. The calculated η_C/η_T for bare GaN based on Eq. (2) agreed well with the measured value of η_C/η_T in Fig. 4(d) based on δ_{GaN} , which demonstrates the usefulness of the phase detection routines in terms of surface scattering. Presuming that spectral attenuation from surface diffuse scattering should be applied equally for all samples, the ZA phonon coupling rate can be inspected by analyzing the constituting components of η_C in the spectral domain after interfacial phonon transfer.

We subsequently reproduced the $\hat{\eta}_C$ spectra for different annealing temperatures with the variable parameter of k_{vdW} , as indicated by the squares (unannealed sample), triangle (200 °C annealed sample), and circle (400 °C annealed sample) in

This is the author's peer reviewed, accepted manuscript. However, the online version of record will be different from this version once it has been copyedited and typeset.
PLEASE CITE THIS ARTICLE AS DOI: 10.1063/5.0069466

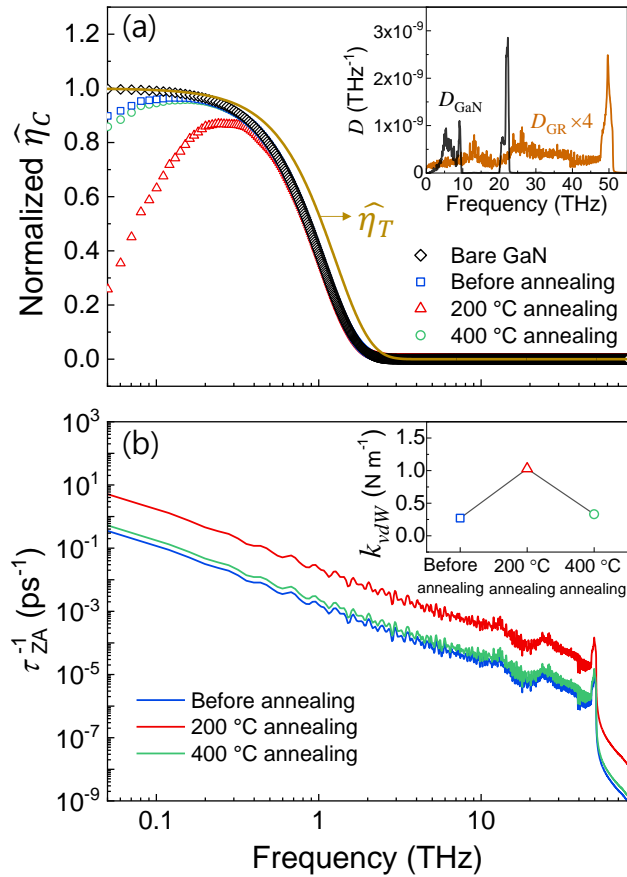


FIG. 5. (a) Estimated spectra of AC wavepackets ($\hat{\eta}_C$) for samples of bare GaN and GaN with graphene after annealing at different temperatures. $\hat{\eta}_C$ for each sample is indicated by scatter compared to the broader spectrum of $\hat{\eta}_T$ (yellow solid line). The inset shows the phonon density of states for graphene (D_{GR}) and GaN (D_{GaN}). (b) The flexural acoustic (ZA) phonon coupling rate at the interface (τ_{ZA}^{-1}) as a function of frequency for graphene on GaN after annealing at different temperatures. The inset shows the coupling constant (k_{vdW}) for the graphene/GaN interfaces, estimated based on Eq. (2).

Fig. 5(a). For the samples with graphene, the attenuation up to ~ 500 GHz in $\hat{\eta}_C$ was noticeable compared to that of bare GaN, which reveals the coupling role of the low-frequency components of the ZA mode. The spectral lineshapes were distinguished according to different annealing temperatures, which exposed the k_{vdW} dependence in τ_{ZA}^{-1} . The quantified k_{vdW} at the graphene/GaN interfaces with different annealing temperatures is displayed in the inset of Fig. 5(b). In the sample without annealing, the value of k_{vdW} was ~ 0.27 N m⁻¹, which is the smallest value among the samples. The k_{vdW} value for the sample after annealing at a temperature of 200 °C was significantly increased to ~ 1.03 N m⁻¹. Accordingly, the largest graphene-induced attenuation of $\hat{\eta}_C$ was observed for the sample annealed at a temperature of 200 °C. However, when the annealing temperature was increased to 400 °C, $\hat{\eta}_C$ exhibited a similar spectrum to that of the sample before annealing by decreasing k_{vdW} (~ 0.33 N m⁻¹). In this manner, our approach based on the spectral evolution of $\hat{\eta}_C$ with different anneal-

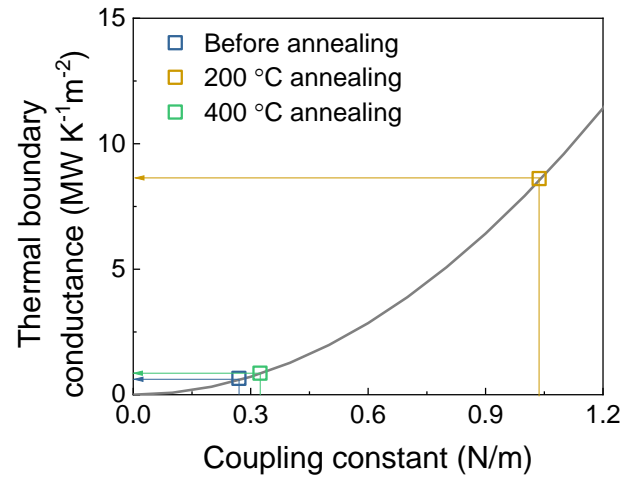


FIG. 6. Thermal boundary conductance calculated at 300 K according to the coupling constants (k_{vdW}) for graphene/GaN interface with different annealing temperature.

ing temperatures has important implications for the interfacial properties.

Previously, Chen *et al.*⁵⁵ quantified the k_{vdW} of 0.12 N m⁻¹ for the unannealed graphene/GaN interface that was fabricated by the PMMA-assisted transfer method, whose value was ~ 2 times smaller than our minimum value without annealing. Such deviation in k_{vdW} has also been found in graphene/SiO₂ interfaces, which have been extensively investigated; Ishigami *et al.*⁵⁶ measured the k_{vdW} of 0.4 N m⁻¹ in the context of adhesion energy measurements of graphene on SiO₂. In contrast, Yasaei *et al.*⁵⁷ reported much larger k_{vdW} value of 2.25 N m⁻¹ for graphene/SiO₂ from the Ti/graphene/SiO₂ interface. The value of k_{vdW} from Yasaei *et al.*⁵⁷ is similar to the follow-up calculations⁵⁸ for graphene/a-SiO₂ with perfectly flat graphene and a-SiO₂ surfaces.

Typically, k_{vdW} is formulated as a function of the separation distance (h_0) between the perfectly flat graphene and substrate⁶⁰: $k_{\text{vdW}} \propto -\frac{2}{3}(\frac{h_0}{h})^5 + \frac{5}{3}(\frac{h_0}{h})^{11}$. However, it was not possible to directly examine the influence of the lateral distribution in h_0 on k_{vdW} here. Instead, we estimated k_{vdW} values averaged over the spot size of ultrafast acoustics scheme for graphene with non-uniform morphology on the substrate. Accordingly, this spatial irregularity of the interfacial bonding could possibly lead to uncertainty in k_{vdW} in our estimation. Considering the surface roughness of substrate⁵⁹ or the morphology of graphene layer⁶⁰, the planar mapping of k_{vdW} between graphene and GaN can be further pursued in terms of the spatially inhomogeneous adhesion between graphene and GaN elsewhere.

According to the extracted k_{vdW} values, we estimated τ_{ZA}^{-1} as a function of frequency for different annealing temperatures, as shown in Fig. 5(b). The decreasing tendency in τ_{ZA}^{-1} is mainly due to the dependence on ω^{-2} , whereas τ_{ZA}^{-1} was suppressed abruptly above the cutoff frequency of $D_{\text{GR}} \sim 52$ THz. The estimated τ_{ZA}^{-1} clearly conveys the quadratic depen-

TABLE I. Measured thermal boundary conductance (TBC) between graphene and substrates at 300 K.

	Interface	Materials	TBC (MW K ⁻¹ m ⁻²)
This work before annealing	graphene/GaN	graphene/GaN	0.65
This work after annealing at 200 °C	graphene/GaN	graphene/GaN	8.61
This work after annealing at 400 °C	graphene/GaN	graphene/GaN	0.86
Judek <i>et al.</i> ⁶¹	graphene/SiO ₂	graphene/SiO ₂ /Si	1.7
Freitag <i>et al.</i> ⁴	graphene/SiO ₂	graphene/SiO ₂	23.8
Vaziri <i>et al.</i> ⁶²	graphene/SiO ₂	graphene/SiO ₂ /Si	27
Mak <i>et al.</i> ⁶³	graphene/SiO ₂	graphene/SiO ₂	50
Yang <i>et al.</i> ⁶⁴	graphene/SiO ₂	Au/Ti/graphene/SiO ₂	42
Chen <i>et al.</i> ⁶⁵	graphene/SiO ₂	Au/SiO ₂ /graphene/SiO ₂ /Si	83.33–178.57
Zhao <i>et al.</i> ⁶⁶	corrugated graphene/SiO ₂	graphene/SiO ₂	340 × 10 ⁻⁶

dence of k_{vdw} , suggesting that the phonon transfer rate from GaN to graphene can be increased with the improvement of the interfacial bonding properties. Even though D_{GR} is another key parameter determining τ_{ZA}^{-1} , the effect of wrinkling on D_{GR} of graphene has been known to be insignificant below ~ 30 THz¹³ and thus is reasonably negligible in the thermally important frequency bands.

Using the estimated τ_{ZA}^{-1} , we then evaluated the thermal boundary conductance (TBC) of the graphene/GaN interface, which can be expressed as⁵⁴ $G(T) = \int_0^\infty \hbar \omega \tau_{\text{ZA}}^{-1}(\omega) D_{\text{GaN}}(\omega) \frac{df_{\text{B-E}}(\omega, T)}{dT} d\omega$. Figure 6 demonstrates TBC values at 300 K as a function of k_{vdw} , indicated by the gray solid line. It can be seen that TBC increases with quadratic dependence on coupling constant ($\propto k_{\text{vdw}}^2$). The values of TBC according to k_{vdw} for graphene/GaN interface with different annealing temperatures were then represented as scatters. The TBC at graphene/GaN interface before annealing was estimated to be ~ 0.65 MW K⁻¹m⁻². After thermal annealing, TBC was increased to ~ 8.61 MW K⁻¹m⁻² (for 200 °C) and ~ 0.86 MW K⁻¹m⁻² (for 400 °C), respectively. Notably, the TBC after annealing at 200 °C was significantly increased to ~ 8.61 MW K⁻¹m⁻² compared with the sample before annealing. On the other hand, the TBC for the sample after annealing at 400 °C was reduced back to the value similar to the sample without annealing due to the occurrence of delamination underneath the wrinkle.

Because of the lacking reports on TBC at graphene/GaN interface, our TBC values were instead compared with TBC values for graphene/SiO₂, as summarized in Table 1. In general, the TBC values for the graphene/GaN interface in our estimation were relatively low compared to the reported values for graphene/SiO₂ interfaces, which could be ascribed to the difference between the specific heats of the substrates derived from the phonon DOS. Interestingly, the TBC of 1.7 MW K⁻¹m⁻² for the graphene/SiO₂ interface reported by Judek *et al.*⁶¹ was similar to our estimation for the graphene/GaN interface after annealing at 200 °C. Notably, Chen *et al.*⁶⁵ reported a much larger TBC of 83.33–178.57 MW K⁻¹m⁻² for the graphene/SiO₂ interface, which was measured from the graphene embedded between SiO₂ layers. This embedded structure could have minimized the delamination character of graphene layer, which concomitantly maximized k_{vdw} .

Another possibility is that adhesion of graphene could be improved by annealing, which is inherently involved in the fabrication of SiO₂/graphene/SiO₂ structure. In clear contrast to the measured TBC values for graphene layers with minimal delamination from the substrate surface, Zhao *et al.*⁶⁶ reported an extremely low TBC of $\sim 340 \times 10^{-6}$ MW K⁻¹m⁻² at corrugated graphene/SiO₂ interface, where the large areas of graphene are poorly in contact with the surface of SiO₂. The large deviation of the TBC in the graphene/SiO₂ derivatives is therefore reasonably attributed to the interfacial property. In this regard, the TBC values at the interfaces between various 2D materials and substrates, including the graphene/GaN interface, can be further corroborated by identification of interface-related parameters such as interfacial separation and adhesion energy.

C. Implications of thermal boundary conductance on a macroscopic scale

The reduced surface temperature of electronic¹ and optoelectronic devices³ using graphene-based heat-spreading layers suggested that graphene can enhance the heat dissipation efficiency even though a complicated limitation should be imposed due to different heat dissipation channels through the substrate or thermal emission.⁶⁷ This heat dissipation role of graphene, which has been repeatedly revealed through macroscopic temperature changes, also implies that the macroscopic prediction by Fourier's law may relate to the adhesion properties between graphene and GaN substrates measured in the ballistic phonon transport regime. However, the lack of a compelling link between ultrafast coherent phonon transport and macroscopic concepts based on scattered particles and diffusion probably impinged the most significant limitation to the thermal manipulation of AC phonons. Even when heat diffusion is more relevant for the detection of temperature distribution, the thermal carriers are mainly AC phonons near a few THz. Because phase-sensitive ultrafast acoustics can measure phonon reflection/transmission as a function of their interfacial coupling properties, it will offer a deeper understanding of heat dissipation at the nanoscale as far as the detection scheme for thermally important phonon spectra can be included. In this context, our results for TBC at the graphene/GaN inter-

face demonstrated that thermal annealing can significantly affect macroscopic thermal management⁶⁸, as well as the coherent phononic transport in the ballistic regime represented by the phase shift of AC oscillations at the interfaces.

Intriguingly, ultrafast acoustics measurement techniques have not been fully combined with advances in thermal conductivity measurement based on time-domain thermoreflectance⁶⁹, understood in the context of the spectral contribution of thermally important phonon branches. As this sort of integration of different phononic measurements would be able to present complementary aspects of the phonon transport pathways, it could possibly hint at a comprehensive relevance between coherent phonon transport at scales smaller than the phonon mean free path^{46,47} and macroscopic phenomena based on phenomenological parameters such as thermal conductivity and temperature gradient. Such a multidisciplinary understanding could then be useful in enhancing the performance of heat dissipation systems, thus improving the efficiency of small-scale devices that possess issues regarding waste heat generation by suitably channeling the phononic transfer rates.

IV. CONCLUSIONS

In conclusion, we demonstrated that the TBC at the interfaces of graphene/LEDs can be enhanced by the application of annealing treatments. The phase shift of the AC phonon oscillations in the differential reflectivity spectra was measured as a function of the thermal annealing temperature. Analysis of the corresponding reflection coefficients revealed that AC phonons originating from the quantum wells of the LEDs were most efficiently transferred to the graphene layer after annealing at 200 °C. Our model quantitatively extracted the annealing dependence of the vdW coupling constants based on the phonon reflection coefficient, which exposed the contribution from broad flexural phonon branches to TBC enhancement in the 200 °C annealed sample. Our study sheds new light on the promising role of thermal annealing in improving the interfacial heat transfer rate.

ACKNOWLEDGMENT

This research was supported by Korea Electric Power Corporation (R17XA05-64), the Basic Science Research Program through the National Research Foundation of Korea (NRF) funded by the Ministry of Science, ICT & Future Planning (2018R1A2B6008101) and the Ministry of Education (2021R1I1A2059710).

AUTHOR DECLARATIONS

The authors have no conflicts to disclose.

Appendix A: Calculation method of phonon density of states

We performed molecular dynamics simulation using the graphics processing units molecular dynamics (GPUMD) package⁷⁰ to calculate the phonon DOS of graphene and bulk GaN. The structure size of graphene was set as 12.546 nm × 21.726 nm ($x \times y$), and the periodic boundary condition was applied to the in-plane directions. The bulk GaN was built with a size of 4.18 nm × 7.24 nm × 5.24 nm ($x \times y \times z$). The Tersoff-type potentials^{71,72} were used to describe the covalent C-C bond of graphene and Ga-N of GaN. The simulation system of graphene was equilibrated for 1 ns, which allowed perfectly flat graphene without strain and wrinkle. The structure was simulated for 20 ns with a time step of 0.5 fs. The phonon DOS ($D(\omega)$) was calculated from the Fourier transform of the velocity autocorrelation function, which is given as $D(\omega) = \frac{1}{3Nk_B T} \int \frac{\langle \vec{v}(t) \cdot \vec{v}(0) \rangle}{\langle \vec{v}(0) \cdot \vec{v}(0) \rangle}$, where ω is the frequency, $\langle \vec{v}(t) \cdot \vec{v}(0) \rangle$ is the velocity autocorrelation function, N is the number of atoms, k_B is the Boltzmann constant, and T is the absolute temperature.

DATA AVAILABILITY

The data that support the findings of this study are available from the corresponding authors upon reasonable request.

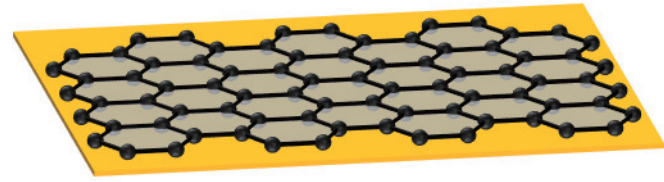
REFERENCES

- Z. Yan, G. Liu, J. M. Khan, and A. A. Balandin, Nat. Commun. **3**, 827 (2012).
- R. Prasher, Science **9**, 185 (2010).
- N. Han, T. V. Cuong, M. Han, B. D. Ryu, S. Chandramohan, J. B. Park, J. H. Kang, Y.-J. Park, K. B. Ko, H. Y. Kim, H. K. Kim, J. H. Ryu, Y. S. Katharria, C.-J. Choi, and C.-H. Hong, Nat. Commun. **4**, 1452 (2013).
- M. Freitag, M. Steiner, Y. Martin, V. Perebeinos, Z. Chen, J. C. Tsang, and P. Avouris, Nano Lett. **9**, 1883 (2009).
- A. A. Balandin, S. Ghosh, W. Bao, I. Calizo, D. Teweldebrhan, F. Miao, and C. N. Lau, Nano Lett. **8**, 902 (2008).
- J. H. Seol, I. Jo, A. L. Moore, L. Lindsay, Z. H. Aitken, M. T. Pettes, X. Li, Z. Yao, R. Huang, D. Broido, N. Mingo, R. S. Ruoff, and L. Shi, Science **328**, 213 (2010).
- H. Malekpour, P. Ramnani, S. Srinivasan, G. Balasubramanian, D. L. Nika, A. Mulchandani, R. K. Lake, and A. A. Balandin, Nanoscale **8**, 14608, (2016).
- S. Chen, Q. Wu, C. Mishra, J. Kang, H. Zhang, K. Cho, W. Cai, A. A. Balandin, and R. S. Ruoff, Nat. Mater. **11**, 203 (2012).
- H. Li, H. Ying, X. Chen, D. L. Nika, A. I. Cocemasov, W. Cai, A. A. Balandin, and S. Chen, Nanoscale **6**, 13402 (2014).
- J. C. Meyer, A. K. Geim, M. I. Katsnelson, K. S. Novoselov, T. J. Booth, and S. Roth, Nature **446**, 60 (2007).
- W. Bao, F. Miao, Z. Chen, H. Zhang, W. Jang, C. Dames, and C. N. Lau, Nat. Nanotechnol. **4**, 562 (2009).
- W. Wang, S. Yang, and A. Wang, Sci. Rep. **7**, 8244 (2017).
- L. Cui, X. Du, G. Wei, and Y. Feng, J. Phys. Chem. C **120**, 23807 (2016).
- C. Wang, Y. Liu, L. Li, and H. Tan, Nanoscale **6**, 5703 (2014).
- A. Mohapatra, S. Das, K. Majumdar, M. S. R. Rao, and M. Jaiswal, Nanoscale Adv. **3**, 1708 (2021).
- A. Pirkle, J. Chan, A. Venugopal, D. Hinojos, C. W. Magnuson, S. McDonnell, L. Colombo, E. M. Vogel, R. S. Ruoff, and R. M. Wallace, Appl. Phys. Lett. **99**, 122108 (2011).

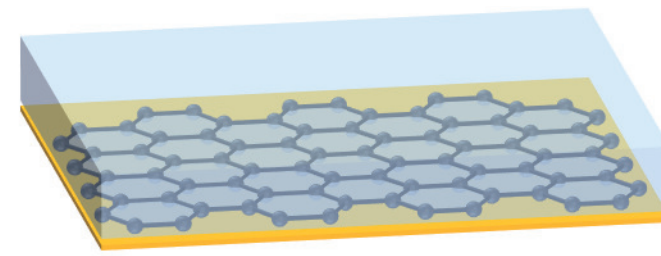
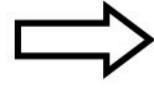
This is the author's peer reviewed, accepted manuscript. However, the online version of record will be different from this version once it has been copyedited and typeset.
PLEASE CITE THIS ARTICLE AS DOI: 10.1063/5.0069466

- ¹⁷X. Du, I. Skachko, A. Barker, E. Y. Andrei, *Nat. Nanotechnol.* **3**, 491 (2008).
- ¹⁸Z. Cheng, Q. Zhou, C. Wang, Q. Li, C. Wang, and Y. Fang, *Nano Lett.* **11**, 767 (2011).
- ¹⁹H. Jeong, Y. D. Jho, and C. J. Stanton, *Phys. Rev. Lett.* **114**, 043603 (2015).
- ²⁰H. Jeong, Y. D. Jho, S. H. Rhim, K. J. Yee, S. Y. Yoon, J. P. Shim, D. S. Lee, J. W. Ju, J. H. Baek, and C. J. Stanton, *Phys. Rev. B* **94**, 024307 (2016).
- ²¹G. Wang, L. Liu, Z. Dai, Q. Liu, H. Miao, and Z. Zhang, *Carbon* **86**, 69 (2015).
- ²²T. Jiang, Z. Wang, X. Ruan, and Y. Zhu, *2D Mater.* **6**, 015026 (2019).
- ²³W. Zhu, T. Low, V. Perebeinos, A. A. Bol, Y. Zhu, H. Yan, J. Tersoff, and P. Avouris, *Nano Lett.* **12**, 7, 3431 (2012).
- ²⁴D. Yoon, Y.-W. Son, and H. Cheong, *Nano Lett.* **11**, 3227 (2011).
- ²⁵R. R. Reeber and K. Wang, *J. Mater. Res.* **15**, 40 (2000).
- ²⁶J. Zabel, R. R. Nair, A. Ott, T. Georgiou, A. K. Geim, K. S. Novoselov, and C. Casiraghi, *Nano Lett.* **12**, 617 (2012).
- ²⁷V. Yu and M. Hilke, *Appl. Phys. Lett.* **95**, 151904 (2009).
- ²⁸A. C. Ferrari and D. M. Basko, *Nat. Nanotechnol.* **8**, 235 (2013).
- ²⁹P. Wang, W. Gao, and R. Huang, *J. Appl. Phys.* **119**, 074305 (2016).
- ³⁰K. Zhang and M. Arroyo, *J. Appl. Phys.* **113**, 193501 (2013).
- ³¹T. Journot, H. Okuno, N. Mollard, A. Michon, R. Dagher, P. Gergaud, J. Dijon, A. V. Kolobov, and B. Hyot, *Nanotechnology* **30**, 505603 (2019).
- ³²C. Thomsen, H. T. Grahn, H. J. Maris, J. Tauc, and J. J. Hauser, *Phys. Rev. Lett.* **53**, 989 (1984); C. Thomsen, H. T. Grahn, H. J. Maris, and J. Tauc, *Phys. Rev. B* **34**, 4129 (1986).
- ³³R. Liu, G. D. Sanders, C. J. Stanton, C. S. Kim, J. S. Yahng, Y. D. Jho, K. J. Yee, E. Oh, and D. S. Kim, *Phys. Rev. B* **72**, 195335 (2005).
- ³⁴J. D. G. Greener, A. V. Akimov, V. E. Gusev, Z. R. Kudrynskiy, P. H. Beton, Z. D. Kovalyuk, T. Taniguchi, K. Watanabe, A. J. Kent, and A. Patané, *Phys. Rev. B* **98**, 075408 (2018).
- ³⁵J. D. G. Greener, E. de L. Savi, A. V. Akimov, S. Raetz, Z. Kudrynskiy, Z. D. Kovalyuk, N. Chigarev, A. Kent, A. Patané, and V. Gusev, *ACS Nano* **13**, 11530 (2019).
- ³⁶H.-Y. Chen, Y.-R. Huang, H.-Y. Shih, M.-J. Chen, J.-K. Sheu, and C.-K. Sun, *Appl. Phys. Lett.* **111**, 213101 (2017).
- ³⁷C.-K. Sun, Y.-T. Yao, C.-C. Shen, M.-H. Ho, T.-C. Lu, and J.-K. Sheu, *J. Phys. Chem. C* **124**, 2987 (2020).
- ³⁸K.-Y. Chou, C.-L. Wu, C.-C. Shen, J.-K. Sheu, and C.-K. Sun, *J. Phys. Chem. C* **125**, 3134 (2021).
- ³⁹S. Lee, H. Jeong, H. Lee, A. J. Minnich, S.-R. Jeon, T. H. Chung, C. J. Stanton, and Y. D. Jho, arXiv:1803.02105v3.
- ⁴⁰S. Wu, P. Geiser, J. Jun, J. Karpinski, and R. Sobolewski, *Phys. Rev. B* **76**, 085210.
- ⁴¹P. Soubelet, A. A. Reynoso, A. Fainstein, K. Nogajewski, M. Potemski, C. Faugeras, and A. E. Bruchhausen, *Nanoscale* **11**, 10446 (2019).
- ⁴²P.-A. Mante, Y.-R. Huang, S.-C. Yang, T.-M. Liu, A. Maznev, J.-K. Sheu, and C.-K. Sun, *Ultrasonics* **56**, 52 (2015).
- ⁴³T.-H. Chou, L. Lindsay, A. A. Maznev, J. S. Gandhi, D. W. Stokes, R. L. Forrest, A. Bensaoula, K. A. Nelson, and C.-K. Sun, *Phys. Rev. B* **100**, 094302 (2019).
- ⁴⁴T.-M. Liu, S.-Z. Sun, C.-F. Chang, C.-C. Pan, G.-T. Chen, J.-I. Chyi, V. Gusev, and C.-K. Sun, *Appl. Phys. Lett.* **90**, 041902 (2007).
- ⁴⁵A. A. Maznev, F. Hofmann, A. Jandl, K. Esfarjani, M. T. Bulsara, E. A. Fitzgerald, G. Chen, and K. A. Nelson, *Appl. Phys. Lett.* **102**, 041901 (2013).
- ⁴⁶A. J. Minnich, J. A. Johnson, A. J. Schmidt, K. Esfarjani, M. S. Dresselhaus, K. A. Nelson, and G. Chen, *Phys. Rev. Lett.* **107**, 095901 (2011).
- ⁴⁷M. Maldovan, *Nat. Mater.* **14**, 667 (2015).
- ⁴⁸E. T. Swartz and R. O. Pohl, *Rev. Mod. Phys.* **61**, 605 (1989).
- ⁴⁹R. Prasher, *Appl. Phys. Lett.* **94**, 041905 (2009).
- ⁵⁰Z.-Y. Ong and E. Pop, *Phys. Rev. B* **84**, 075471 (2011).
- ⁵¹G. C. Correa, C. J. Foss, and Z. Aksamija, *Nanotechnology* **28**, 135402 (2017).
- ⁵²J. M. Ziman, *Electrons and Phonons: The Theory of Transport Phenomena in Solids*, Oxford University Press, Oxford, UK, 1960.
- ⁵³Y.-C. Wen, C.-L. Hsieh, K.-H. Lin, H.-P. Chen, S.-C. Chin, C.-L. Hsiao, Y.-T. Lin, C.-S. Chang, Y.-C. Chang, L.-W. Tu, and C.-K. Sun, *Phys. Rev. Lett.* **103**, 264301 (2009).
- ⁵⁴C. J. Foss and Z. Aksamija, *2D Mater.* **6**, 025019 (2019).
- ⁵⁵I.-J. Chen, P.-A. Mante, C.-K. Chang, S.-C. Yang, H.-Y. Chen, Y.-R. Huang, L.-C. Chen, K.-H. Chen, V. Gusev, and C.-K. Sun, *Nano Lett.* **14**, 1317 (2014).
- ⁵⁶M. Ishigami, J. H. Chen, W. G. Cullen, M. S. Fuhrer, and E. D. Williams, *Nano Lett.* **7**, 1643 (2007).
- ⁵⁷P. Yasaei, C. J. Foss, K. Karis, A. Behranginia, A. I. El-Ghandour, A. Fathizadeh, J. Olivares, A. K. Majee, C. D. Foster, F. Khalili-Araghi, Z. Aksamija, A. Salehi-Khojin, *Adv. Mater. Interfaces* **4**, 1700334 (2017).
- ⁵⁸B. N. J. Persson and H. Ueba, *Europhys. Lett.* **91**, 56001 (2010).
- ⁵⁹W. Gao and R. Huang, *J. Phys. D: Appl. Phys.* **44**, 452001 (2011).
- ⁶⁰Z. H. Aitken and R. Huang, *J. Appl. Phys.* **107**, 123531 (2010).
- ⁶¹J. Judek, A. P. Gertych, M. Swiniarski, A. Lapinska, A. Duzynska, M. Zdrojek, *Sci. Rep.* **5**, 12422 (2015).
- ⁶²S. Vaziri, E. Yalon, M. M. Rojo, S. V. Suryavanshi, H. Zhang, C. J. McClellan, C. S. Bailey, K. K. H. Smithe, A. J. Gabourie, V. Chen, S. Deshmukh, L. Bendersky, A. V. Davydov, E. Pop, *Sci. Adv.* **5**, eaax1325 (2019).
- ⁶³K. F. Mak, C. H. Lui, T. F. Heinz, *Appl. Phys. Lett.* **97**, 221904 (2010).
- ⁶⁴J. Yang, E. Ziade, C. Maragliano, R. Crowder, X. Wang, M. Stefancich, M. Chiesa, A. K. Swan, and A. J. Schmidt, *J. Appl. Phys.* **116**, 023515 (2014).
- ⁶⁵Z. Chen, W. Jang, W. Bao, C. N. Lau, and C. Dames, *Appl. Phys. Lett.* **95**, 161910 (2009).
- ⁶⁶W. Zhao, W. Chen, Y. Yue, S. Wu, *Appl. Therm. Eng.* **113**, 481 (2017).
- ⁶⁷See, e.g., R.-J. Shiue, Y. Gao, C. Tan, C. Peng, J. Zheng, D. K. Efetov, Y. D. Kim, J. Hone, and D. Englund, *Nat. Commun.* **10**, 109 (2019).
- ⁶⁸Y. Li, Y. Zhu, G. Jiang, Z. P. Cano, J. Yang, J. Wang, J. Liu, X. Chen, and Z. Chen, *Small* **16**, 1903315 (2020).
- ⁶⁹D. G. Cahill, P. V. Braun, G. Chen, D. R. Clarke, S. Fan, K. E. Goodson, P. Keblinski, W. P. King, G. D. Mahan, A. Majumdar, H. J. Maris, S. R. Phillpot, E. Pop, and L. Shi, *Appl. Phys. Rev.* **1**, 011305 (2014).
- ⁷⁰Z. Fan, W. Chen, V. Vierimaa, and A. Harju, *Comput. Phys. Commun.* **218**, 10 (2017).
- ⁷¹J. Nord, K. Albe, P. Erhart, and K. Nordlund, *J. Phys.: Condens. Matter* **15**, 5649 (2003).
- ⁷²L. Lindsay and D. A. Broido, *Phys. Rev. B* **81**, 205441 (2010).

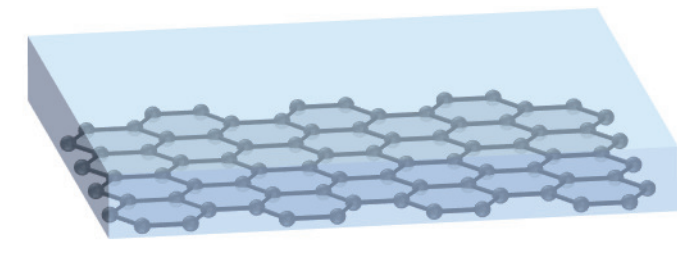
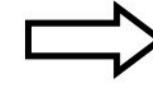
This is the author's peer reviewed, accepted manuscript. However, the online version of record will be different from this version once it has been copyedited and typeset.
PLEASE NOTE THIS ARTICLE AS DOI: 10.1063/1.50069466



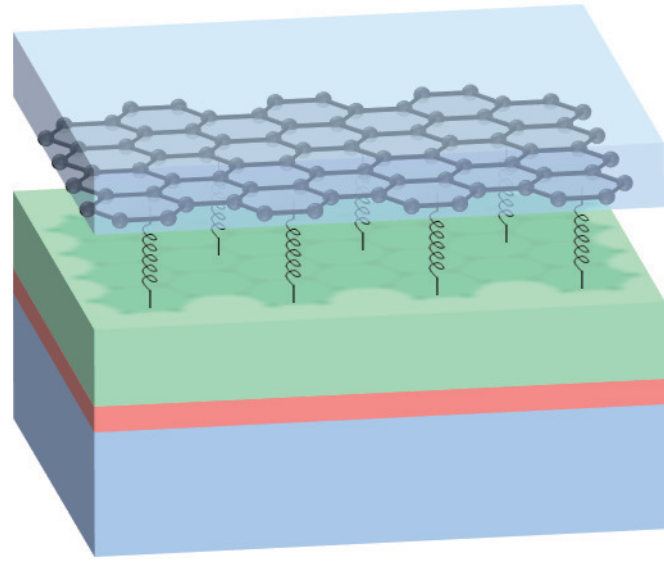
(a) Graphene on Cu foil



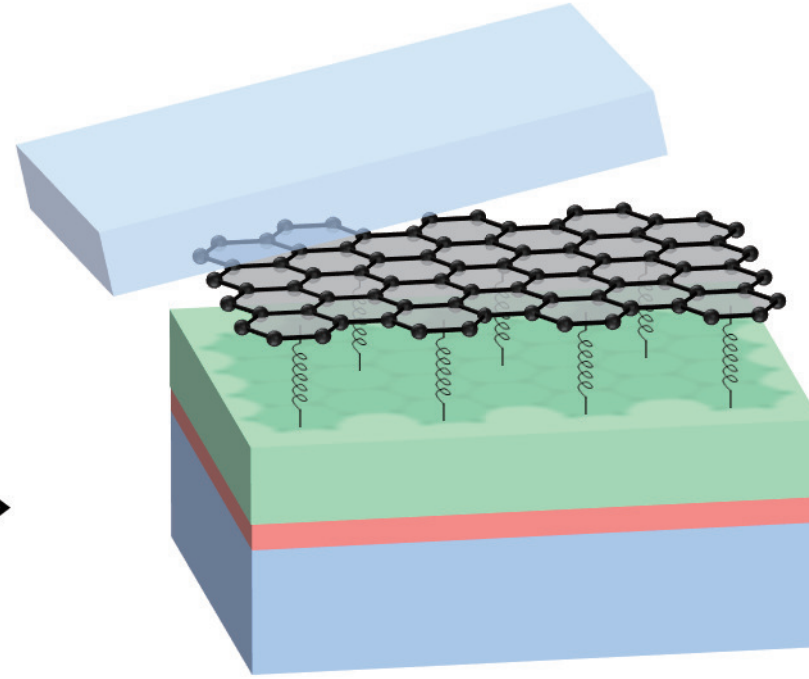
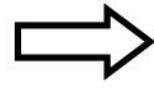
(b) PMMA spin-coated onto the graphene



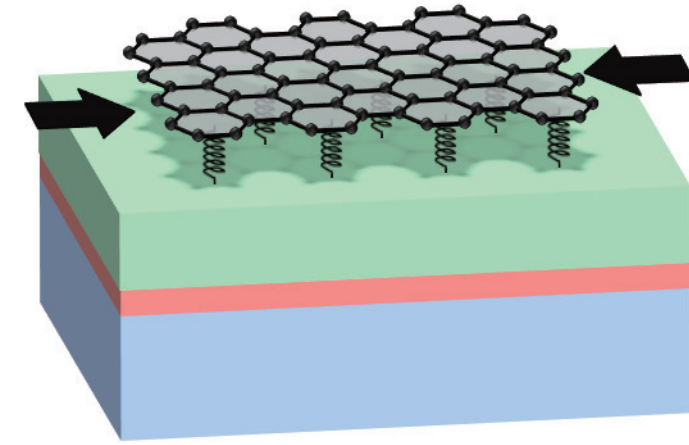
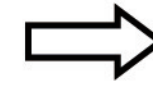
(c) Removal of Cu foil



(d) PMMA/graphene transferred to LEDs

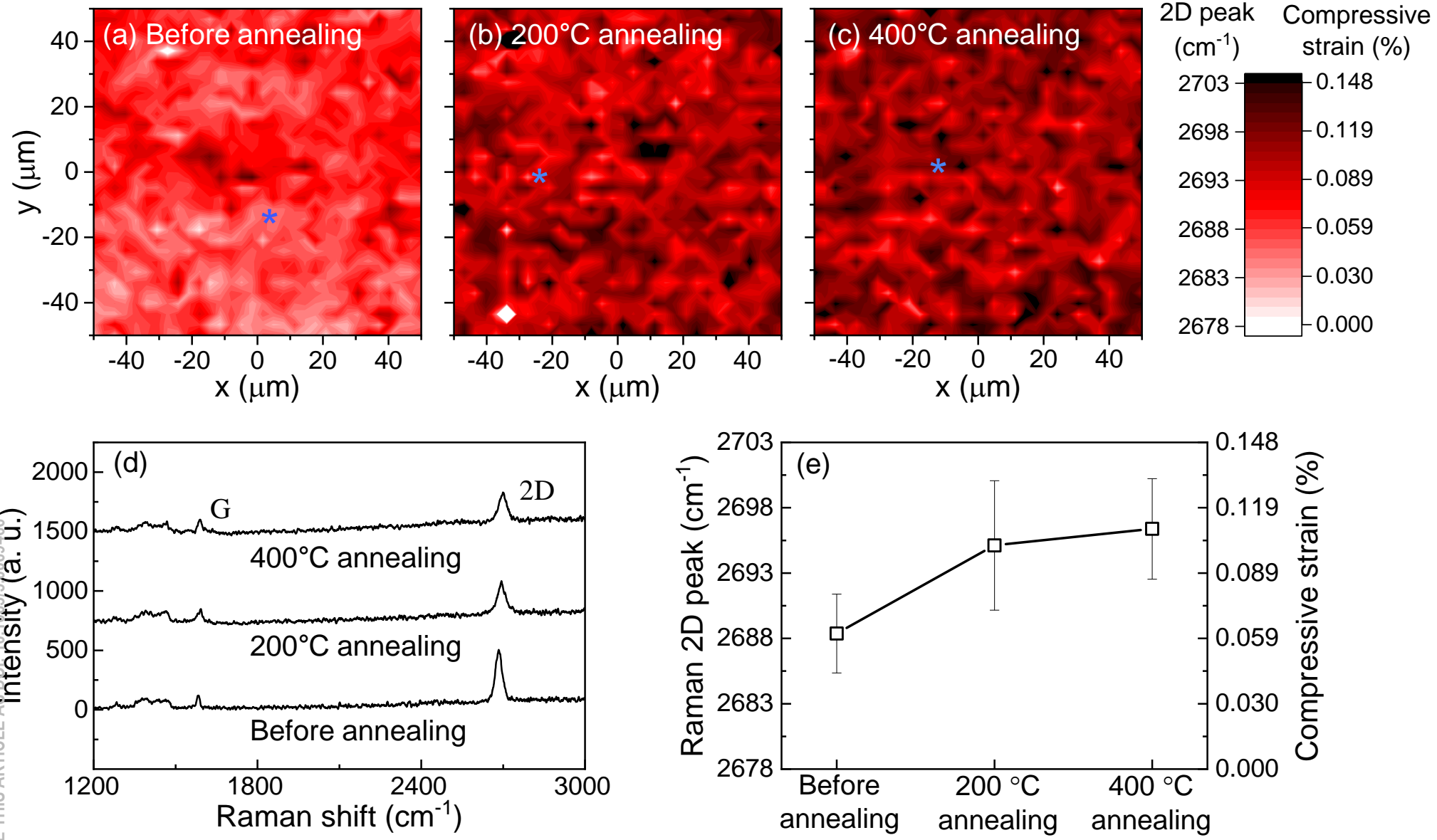


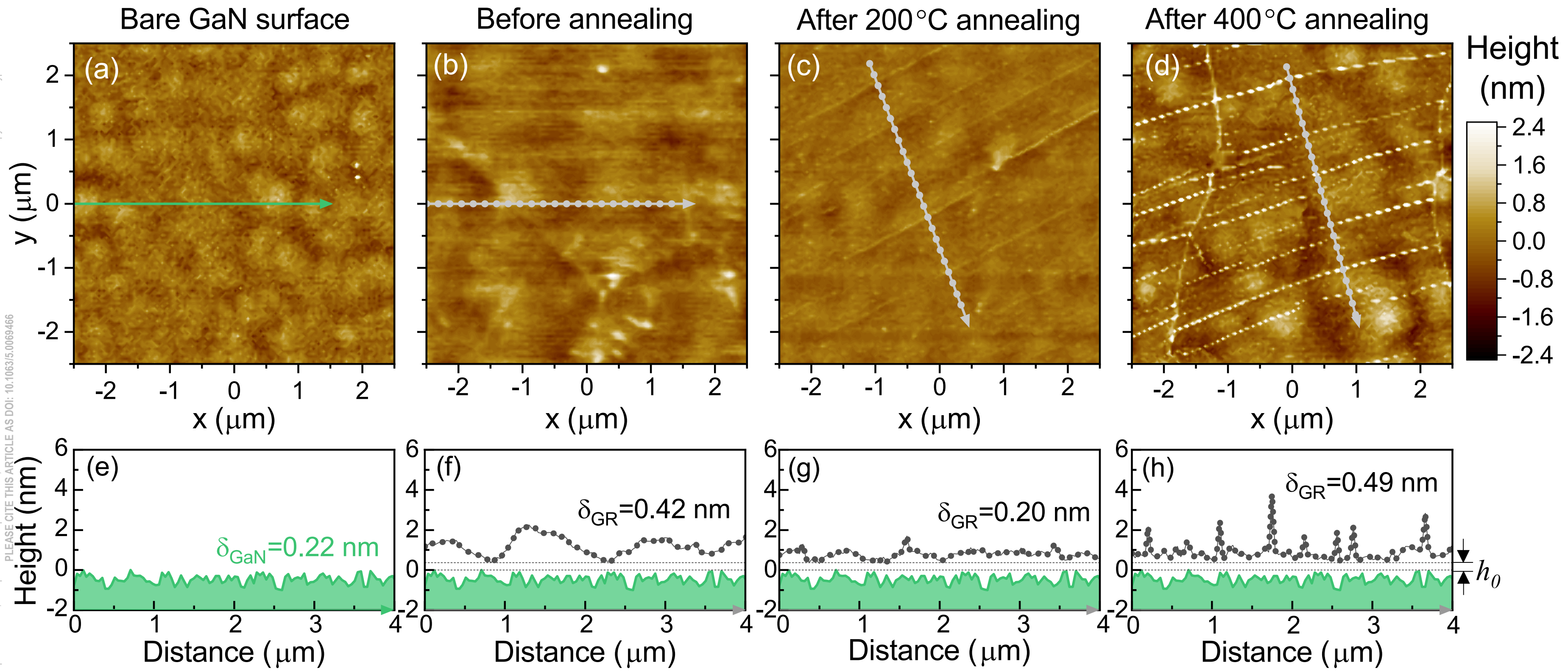
(e) Removal of the PMMA



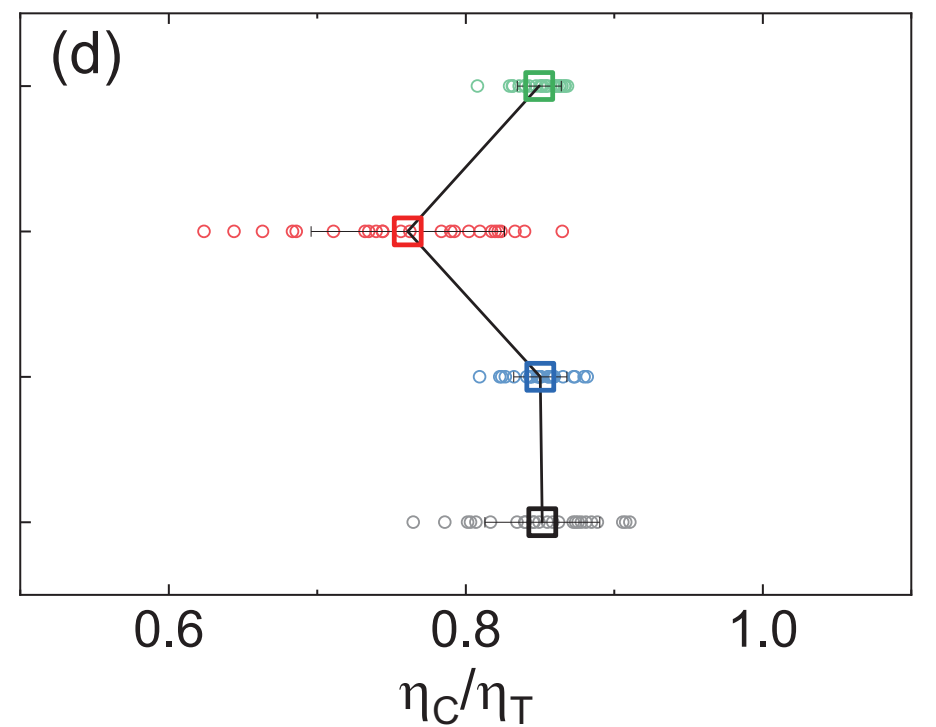
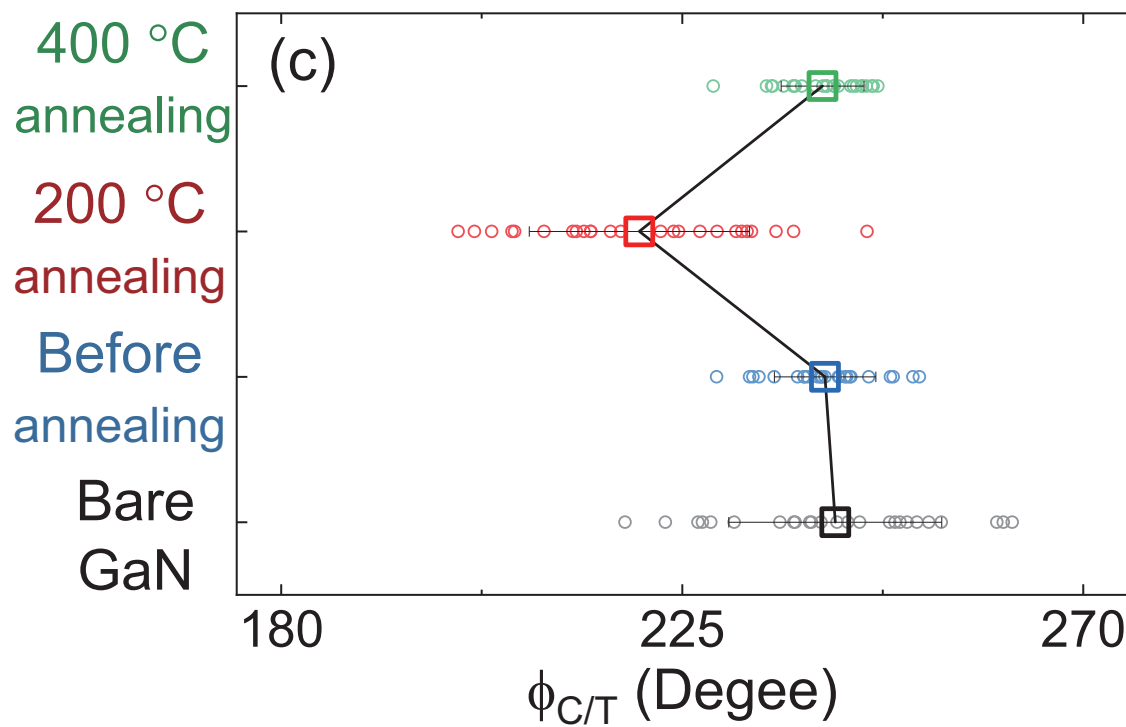
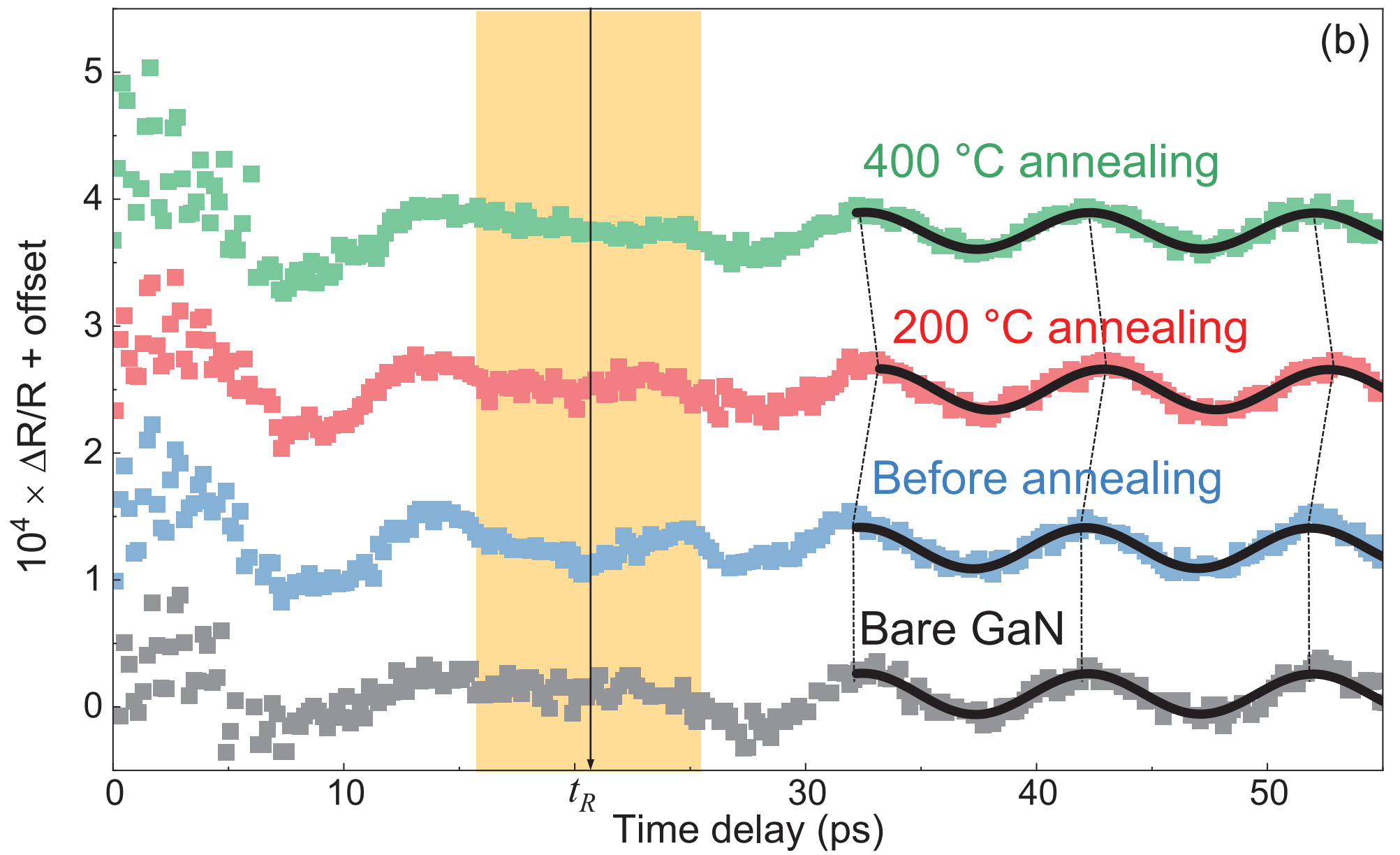
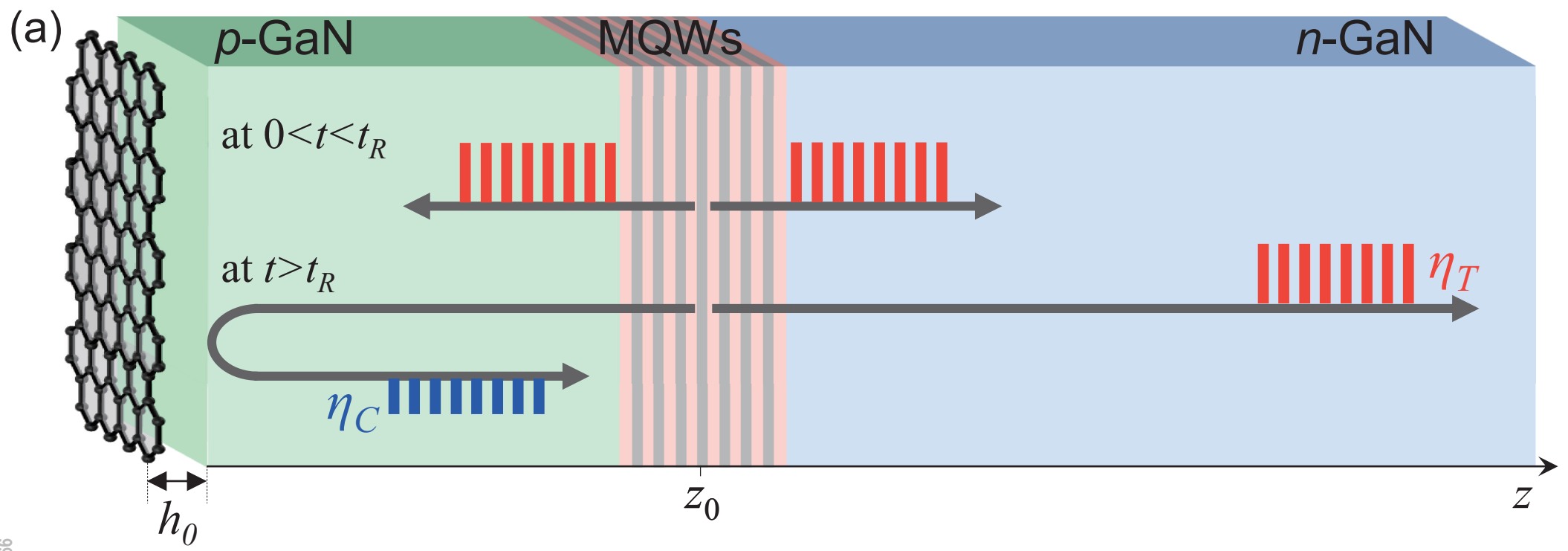
(f) Thermal annealing

This is the author's peer reviewed, accepted manuscript. However, the online version of record will be different from this version once it has been copyedited and typeset.
PLEASE CITE THIS ARTICLE AS DOI: 10.1063/1.50069466

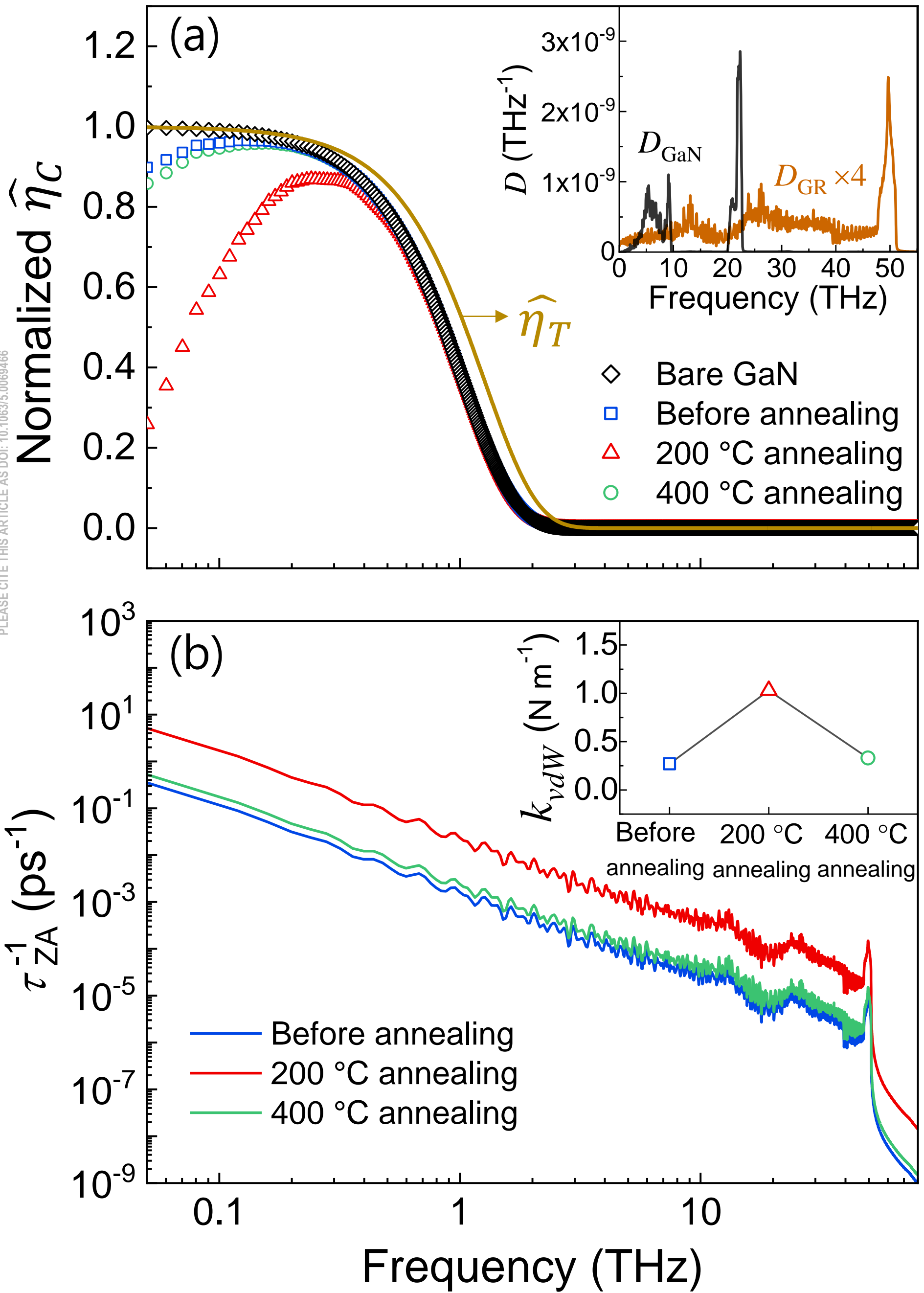




This is the author's peer reviewed, accepted manuscript. However, the online version of record will be different from this version once it has been copyedited and typeset.
PLEASE CITE THIS ARTICLE AS DOI: 10.1063/5.0069466



This is the author's peer reviewed, accepted manuscript. However, the online version of record will be different from this version once it has been copyedited and typeset.
PLEASE CITE THIS ARTICLE AS DOI: 10.1063/5.0069466



This is the author's peer reviewed, accepted manuscript. However, the online version of record will be different from this version once it has been copyedited and typeset.
PLEASE CITE THIS ARTICLE AS DOI: 10.1063/5.0069466

